Research Paper

A Tumor-Activatable Theranostic Nanomedicine Platform for NIR Fluorescence-Guided Surgery and Combinatorial Phototherapy

Xiaoning Li[1], Canan Schumann[1], Hassan A. Albarqi[1], Christopher J. Lee[1], Adam W. G. Alani[1], Shay Bracha[2], Milan Milovancev[2], Olena Taratula[1✉] and Oleh Taratula[1✉]

1. Department of Pharmaceutical Sciences, College of Pharmacy, Oregon State University, Portland, OR 97201, United States;
2. Department of Clinical Sciences, College of Veterinary Medicine, Oregon State University, Corvallis, OR 97331, United States.

✉ Corresponding authors: Oleh.Taratula@oregonstate.edu. Olena.Taratula@oregonstate.edu.

Abstract

Fluorescence image-guided surgery combined with intraoperative therapeutic modalities has great potential for intraoperative detection of oncologic targets and eradication of unresectable cancer residues. Therefore, we have developed an activatable theranostic nanoplatform that can be used concurrently for two purposes: (1) tumor delineation with real-time near infrared (NIR) fluorescence signal during surgery, and (2) intraoperative targeted treatment to further eliminate unresected disease sites by non-toxic phototherapy.

Methods: The developed nanoplatform is based on a single agent, silicon naphthalocyanine (SiNc), encapsulated in biodegradable PEG-PCL (poly (ethylene glycol)-*b*-poly(ε-caprolactone)) nanoparticles. It is engineered to be non-fluorescent initially via dense SiNc packing within the nanoparticle's hydrophobic core, with NIR fluorescence activation after accumulation at the tumor site. The activatable nanoplatform was evaluated *in vitro* and in two different murine cancer models, including an ovarian intraperitoneal metastasis-mimicking model. Furthermore, fluorescence image-guided surgery mediated by this nanoplatform was performed on the employed animal models using a Fluobeam® 800 imaging system. Finally, the phototherapeutic efficacy of the developed nanoplatform was demonstrated *in vivo*.

Results: Our *in vitro* data suggest that the intracellular environment of cancer cells is capable of compromising the integrity of self-assembled nanoparticles and thus causes disruption of the tight dye packing inside the hydrophobic cores and activation of the NIR fluorescence. Animal studies demonstrated accumulation of activatable nanoparticles at the tumor site following systemic administration, as well as release and fluorescence recovery of SiNc from the polymeric carrier. It was also validated that the developed nanoparticles are compatible with the intraoperative imaging system Fluobeam® 800, and nanoparticle-mediated image-guided surgery provides successful resection of cancer tumors. Finally, *in vivo* studies revealed that combinatorial phototherapy mediated by the nanoparticles could efficiently eradicate chemoresistant ovarian cancer tumors.

Conclusion: The revealed properties of the activatable nanoplatform make it highly promising for further application in clinical image-guided surgery and combined phototherapy, facilitating a potential translation to clinical studies.

Key words: NIR theranostic, activatable, silicon naphthalocyanine, PEG-PCL, ovarian cancer.

Introduction

Advanced imaging techniques developed in recent years have promoted insightful understandings of cancer anatomy, metabolism, and biochemistry [1]. The revealed information such as cancer origin, morphology, and invasiveness is extremely crucial for cancer diagnosis and treatment [2-4]. Notably, optical imaging can provide visualization of tumor structures in real-time during cytoreductive surgery [5, 6]. The degree of cytoreduction and the size of residual tumors are closely related to the prediction of cancer recurrence and patient prognosis [7, 8]. Even with the best surgical techniques, however, surgeons still rely on palpation and visual inspection for identification of malignant tissues intraoperatively, which can result in residual tumors [9]. Fluorescence image-guided surgery has a great potential for intraoperative detection of oncologic targets and real-time assessment of tumor borders, thus promising complete tumor resection and improved patient survival rates [10]. Furthermore, it has been demonstrated that intraoperative fluorescence imaging techniques could be powerful tools to enhance surgical outcomes and patient prognosis in clinical research cases of multiple cancer types, including ovarian cancer [11], breast cancer [12-14], cervical cancer [15, 16], liver metastasis [17], melanoma [17, 18], and vulvar cancer [19, 20]. If combined with intraoperative therapeutic modalities, this technique could permit additional treatment following cytoreduction to diminish any possible cancer residues. Currently, this theranostic approach —wherein imaging and therapeutic functions are integrated into a single formulation—is of high interest, especially using a single agent featuring multiple functionalities for the fabrication of a smart "all-in-one" theranostic nanomedicine [21].

One of the main challenges in current fluorescence imaging techniques is accomplishing a high cancer-to-normal tissue contrast ratio, which requires minimizing background signal originating from non-malignant tissue. For this reason, *in vivo* fluorescence imaging prefers fluorophores with absorbance and emission in the near-infrared (NIR) region (700-1000 nm) to overcome the photon attenuation in living tissue [22]. Most tissues have minimal absorption and scattering of NIR light and generate little NIR autofluorescence [23]. Hence, NIR probes offer the advantages of enhanced tissue penetration depth and reduced interfering autofluorescence background. Indocyanine green (ICG), for example, an FDA-registered NIR contrast agent, provides a better contrast and increased light tissue penetration at its emission peak wavelength of 820 nm compared to other visible fluorophores [24, 25]. Due to its preferable fluorescence characteristics, ICG is widely utilized in clinical research, especially in NIR fluorescence image-guided oncologic surgery for the identification of solid tumors after intravenous injection [26, 27]. However, the imaging sensitivity gained using current NIR probes such as ICG is still not sufficient [27]. In general, small molecule probes lack cancer specificity, have relatively low tumor accumulation, and feature a short half-life and fast clearance from systemic circulation [28]. In addition, it was reported that ICG is characterized by relatively short tumor retention time and this behavior limits the temporal window in which fluorescence imaging and/or therapy can be performed [29]. Fluorophores encapsulated within nano-delivery vehicles display prolonged systemic circulation, enhanced tumor accumulation, and extended intratumoral retention [30, 31]. However, cancer-to-normal tissue contrast provided by these nanoprobes is dependent upon the clearance of the nanoparticles and encapsulated and released fluorophores from non-malignant tissues, which cause high background signal [31].

To address these limitations, development of tumor-activatable fluorescent nanoprobes is in great demand. This strategy possesses advantages over the always-ON probes since signals are designed to be activated only at tumor/cancer cells, minimizing the background signal from unbound and uncleared probes and maximizing the tumor-to-normal tissue contrast ratio. Reported studies have explored different approaches to develop activatable NIR probes, such as electron rearrangement at a tumor/cancer cell-specific pH [27], conjugation to an energy transfer-pairing molecule or a quenching nanoparticle via a cleavable linker [32], and self-quenching by close proximity [33, 34]. While new fluorophores or nanocarriers have been discovered via synthesis or conjugation processes, simple modifications of already existing NIR probes or nanoplatform formulations avoid the complex and sophisticated production procedures, and could be expected to have a high potential for translation into clinical scenarios. Moreover, this is especially crucial in constructing smart activatable "all-in-one" theranostic nanosystems, because conjugation or modification of a single imaging and therapeutic agent should be capable of tailoring the agent's fluorescence profile without compromising its therapeutic properties and efficacy.

Recently, we reported the development of a simple, single agent-based nanoplatform with promising theranostic properties based on NIR fluorescence imaging and combinatorial

phototherapy [35]. The developed nanoplatform had the required physico-chemical properties to achieve enhanced tumor accumulation after intravenous injection as was confirmed by *in vivo* experiments. Our previously reported nanoplatform, however, exhibited the always-ON fluorescence mode, resulting in simultaneous generation of fluorescence in tumor and other organs, causing a high background signal [35]. This is a crucial limitation of always-ON nanoparticles applied for fluorescence imaging, including image-guided surgery [36]. Therefore, we aimed to solve this problem by developing a nanoplatform that predominantly activates its fluorescence at tumor/cancer cells.

Herein, we describe an activatable theranostic nanoplatform based on i) silicon naphthalocyanine (SiNc), a photostable fluorescence molecule with enhanced absorption in the spectral range of 750 nm to 800 nm, for optical imaging and photothermal treatment of tumors; and ii) poly (ethylene glycol)-*b*-poly(ε-caprolactone) (PEG-PCL), a biodegradable and biocompatible block polymer, as a nanocarrier (Figure 1). The developed activatable (OFF-ON) SiNc polymeric nanoparticles (activatable SiNc-PNPs) are engineered to be non-fluorescent initially due to SiNc self-quenching, but they can be activated inside tumor tissues and cancer cells to be NIR fluorescent for imaging. Two murine tumor models, a subcutaneous and an intraperitoneal xenograft of human ovarian cancer, were employed to test the activatable SiNc-PNP's theranostic activity. Furthermore, using an FDA-approved intraoperative imaging system Fluobeam® 800, fluorescence image-guided surgery was exploited on tumor-bearing mice.

Materials and Methods

Materials

SiNc (silicon 2,3-naphthalocyanine bis (trihexylsilyloxide)) was purchased from Sigma-Aldrich (Milwaukee, WI). PEG–PCL (methoxy poly(ethylene glycol)-*b*-poly(ε-caprolactone), MW: 5k-10k) and HOOC-PEG-PCL (carboxyl poly(ethylene glycol)-*b*-poly(ε-caprolactone), MW: 5k-10k) were purchased from Advanced Polymer Materials Inc. (Montreal, Canada).

Synthesis of SiNc-loaded polymeric nanoparticles

SiNc-based polymeric nanoparticles were prepared via a solvent evaporation method [35, 37]. In general, PEG-PCL (20 mg) and the desired amount of SiNc (0.1, 0.6 (always-ON), or 1.2 (activatable) mg) were dissolved and mixed in tetrahydrofuran (THF) (2 mL). Under constant stirring, saline (2 mL) was then added to the vial. THF was evaporated using a rotary evaporator with a water bath temperature of 40 °C and a rotation speed of 100 rpm. The evaporation followed a three-segment cycle: first at 400 mbar for 7 min, then 320 mbar for 7 min, and finally 200 mbar for 6 min. The final volume of the nanoparticle solution was adjusted to 2 mL with saline and centrifuged at 10,062 rcf for 5 min. The supernatant was then filtered through a 0.2 μm filter (cellulose acetate, VWR International, Radnor, PA) to collect dispersed nanoparticles with desired SiNc loading amounts (0.05, 0.3 (always-ON), and 0.6 (activatable) mg/mL; loading efficiency was calculated by SiNc (mg) / polymer (mg) × 100% = 0.5%, 3%, and 6%, respectively). The preparation and characterization of always-ON SiNc-PNP (0.3 mg/mL loading) and IR780-PNP was reported earlier by our group [30, 35].
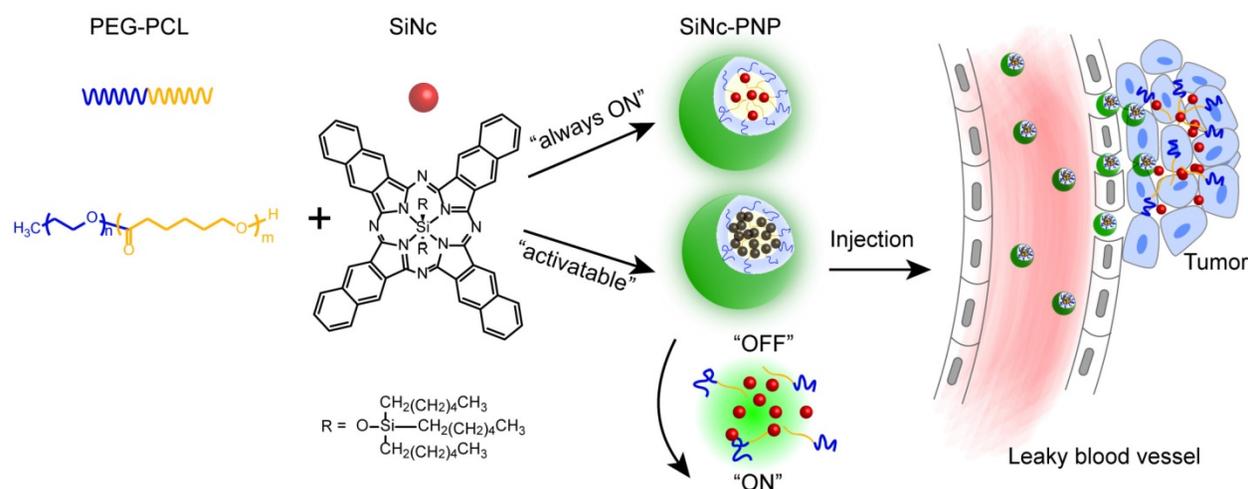

Figure 1. Schematic illustration of the "activatable" and "always-ON" theranostic nanoplatforms. They consist of a NIR theranostic agent, silicon naphthalocyanine (SiNc), and a co-polymer, PEG-PCL, as a nanocarrier. The activatable SiNc-PNP was tailored to be non-fluorescent ("OFF") and maintain "OFF" until reaching the tumor site. Upon intratumoral accumulation, the activatable SiNc-PNPs disintegrate and activate the NIR fluorescence.

Characterization

The absorbance of SiNc-PNPs was recorded on a UV-1800 Shimadzu spectrophotometer (Carlsbad, CA), and fluorescence was measured using a Cary Eclipse R3896 fluorescence Varian spectrophotometer (Mulgrave, Victoria, Australia). The actual SiNc-loadings of SiNc-PNPs were determined by NIR absorption of SiNc at 772 nm and calculated using an extinction coefficient of 472891 $M^{-1}cm^{-1}$. The hydrodynamic diameter, size distribution, and zeta potential of SiNc-PNPs were determined using dynamic light scattering (DLS, Malvern ZetaSizer NanoSeries, Malvern, U.K.). Cryogenic transmission electron microscopy (cryoTEM) was used to characterize SiNc-PNPs morphology and size according to our previously reported procedure [35]. Additional characterization methods are provided in Supplementary Material.

FITC-labelled activatable SiNc-PNP

The fluorescein isothiocyanate (FITC)-labelled activatable SiNc-PNPs were prepared using 1% w/w of FITC-PEG-PCL mixed with non-modified PEG-PCL according to the above described procedure. **FITC-PEG-PCL conjugation:** The HOOC-PEG-PCL (100 mg) was dissolved in 1.6 mL acetonitrile. DCC (N,N'-Dicyclohexylcarbodiimide, 2 mg) was sonicated in acetonitrile (200 μL) for 30 min and then added to the polymer solution, followed by addition of sulfo-NHS (N-hydroxysulfosuccinimide, 12 mg) in acetonitrile (200 μL). ADH (adipic acid dihydrazide, 1.5 mg) was solubilized in PBS (200 μL) at pH 8.2 and added to the polymer mixture solution. The reaction was set at room temperature sonication for 1 h. Excess acetonitrile (5 mL) was added at the end of the reaction to precipitate unreacted ADH and clear supernatant was collected after centrifugation. ADH-PEG-PCL was dried under vacuum and 50 mg was dissolved in 1 mL acetonitrile for the next step. FITC (1.3 mg) in PBS (200 μL, pH 8.2) was added to the polymer solution and stirred for 5 h in the dark. The product was then obtained after dialysis for one week and dried under vacuum.

Cellular uptake and imaging

A2780/CDDP (Developmental Therapeutics Core, Northwestern University, IL) and HEK293 (Sigma-Aldrich) cells (50,000 cells/well) were seeded in a 6-well plate and cultured for 24 h. Cells were incubated with FITC-labeled activatable SiNc-PNP (20 μg/mL of SiNc) in RPMI 1640 (10% fetal bovine serum) for the desired time. Before imaging, cells were washed with PBS. Images were collected with an EVOS FL Cell Imaging System (Life Technologies, Grand Island, NY) using GFP filter cube (Excitation (Ex.) 470/22 nm, Emission (Em.) 510/42 nm) and Cy® 7 filter cube (Ex. 710/40 nm, Em. 775/46 nm). Flow cytometry was employed to evaluate the internalization efficiency of the FITC-labeled activatable SiNc-PNP into A2780/CDDP and HEK293 cells according to our previously published procedure [38].

In vivo imaging in subcutaneous xenograft models

Athymic nude mice (female, 4-6 weeks) were obtained from the Jackson Laboratory (Bar Harbor, ME) and maintained under standard housing conditions. All animal experiments were carried out in accordance with protocols evaluated and approved by Oregon Health & Science University IACUC. In vivo studies were performed in accordance with all national and local guidelines and regulations. Subcutaneous xenograft tumors were derived by inoculation of A2780/CDDP cells (1×10^6 in 100 μL RPMI 1640 and mixed with 100 μL Matrigel) at the lower flank of mice. Tumor growth was monitored and evaluated by tumor sizes calculated as 0.5 × width^2 × length. When tumors reached a volume of ~ 300 mm^3, the activatable SiNc-PNPs (always-ON SiNc-NP and/or IR775 dye in saline with 5% DMSO) were injected into mice via tail vein at a dose of 3.0 mg/kg of dye. The whole animals were imaged using LI-COR Pearl Impulse Imaging System with an 800 nm channel at desired time points. Tumors and organs were dissected from mice 24 h post SiNc-PNP injection and imaged using LI-COR Pearl Impulse Imaging System. Then, regions of interest (ROI) of the same size were drawn over tumor and normal tissue (liver, kidneys, spleen, etc.), and the average fluorescence signal for each area was measured using LI-COR Pearl Impulse Imaging System software. The tumor-to-normal tissue ratio (T/N) was calculated as the ratio between the fluorescence signal in the region of interest within the tumor and the fluorescence signal in the region of interest within the normal tissues including kidneys, liver and lungs. Statistical analysis was performed using Student-t test.

Ex vivo imaging and histology

Tumors were dissected from mice 24 h post SiNc-PNP injection and divided in two. The tumor tissues were then fixed in formalin, embedded in paraffin, sectioned, and collected onto slides as previously reported.[35] Fluorescence imaging was performed with an EVOS FL Cell Imaging System (Life Technologies, Grand Island, NY) using Cy® 7 light cube (Ex. 710/40 nm, Em. 775/46 nm).

Activatable SiNc-PNP mediated image-guided operation

Nude mice bearing subcutaneous xenografts derived from A2780/CDDP were i.v. injected with activatable SiNc-PNP (100 µL, 0.6 mg/mL, 3.0 mg/kg of SiNc) 24 h prior to operation. Animals were euthanized first following IACUC policies and then placed under Fluobeam® 800 supported with a mechanical stand. Dissection of tumors was performed under the guidance of NIR fluorescence signal displayed on a monitor. Real-time videos and images were recorded.

In vivo imaging in intraperitoneal xenograft models

The luciferase-expressing ES-2 (ES-2/Luc) human ovarian cancer cell line was received as a gift from Prof. Glen Kwon, School of Pharmacy-University of Wisconsin. Cells were cultured, harvested, and dispersed in RMPI 1640 and 6×10^6 cells were injected intraperitoneally into athymic nude mice (female, 4-6 weeks). Two weeks post inoculation, the activatable SiNc-PNP were administrated into mice by either i.v. (tail vein) or i.p. injection at a dose of 3.0 mg/kg (SiNc). Mice injected with nanoparticles were housed for 24 h and injected with 200 µL of 15 mg/mL D-luciferin PBS solution 10 min prior to imaging. The whole animals and harvested tumors, heart, liver, spleen, kidneys, and lungs were imaged using an IVIS Lumina XRMS In Vivo Imaging System (PerkinElmer, Waltham, MA). Bioluminescence images were acquired with open emission filter, and NIR fluorescence images were obtained with 780 nm excitation filter and 845 nm emission filter.

In Vivo phototherapy

Nude mice were inoculated subcutaneously with A2780/CDDP cells on both sides, and when tumors reached a size of ~75 mm³, mice were distributed randomly into four groups (3 mice per group, 6 tumors per group). The four groups were assigned as saline injected, saline injected followed with NIR treatment, activatable SiNc-PNP injected, and activatable SiNc-PNP injected followed with NIR treatment. Activatable SiNc-PNP at a dose of 3.0 mg/kg of SiNc or saline were injected into mice via the tail vein. 24 h post-injection, after confirming SiNc-PNP tumor uptake by fluorescence imaging, mice in the NIR treatment assigned groups were treated once with laser (WSLS-785, Wavespectrum Laser Group Limited, China) exposure to the tumors for 10 min on each side (785 nm, 1.3 W/cm²) under anesthesia. After phototherapy, all mice from four groups were monitored for tumor growth and body weight for 16 days when tumors reached a humane point of 1000 mm³.

Intratumoral temperature measurements were carried out on mice bearing similar tumor sizes with those used for phototherapy. Temperature profiles were obtained with a fiber optic probe according to our previously reported procedure. [35] Four choices of NIR laser powers, 0.5, 0.8, 1.1, and 1.3 W/cm², were explored.

Experimental procedures for toxicity studies are provided in Supplementary Material.

Results and Discussion

Synthesis of SiNc-loaded polymeric nanoparticles

Silicon naphthalocyanines (SiNc) have been demonstrated to be promising agents for NIR fluorescence imaging due to their greater photo-stability and quantum yield than ICG [35]. In addition, they possess excellent capability of generating heat for photothermal therapy. Our team recently reported that SiNc molecules can aggregate, leading to fluorescence self-quenching effect [39]. However, with proper axial substituents, permanent SiNc aggregation and corresponding self-quenching can be prevented, and the released molecules in the appropriate environment can potentially provide a high fluorescence signal. Also, due to extremely poor water solubility (<1 ng/mL), the release of nanoparticle-encapsulated SiNc is limited in aqueous environments, which can prevent their leaching from the carriers in systemic circulation, thus minimizing the background signal from released fluorophores [39]. Therefore, we proposed to utilize these features of SiNc to fabricate the tumor-activatable SiNc-PNP. Our hypothesis is that by controlling the SiNc payload into polymeric nanoparticles, the SiNc intermolecular distance could be tailored for close proximity to cause self-quenching and, therefore, diminish NIR fluorescence. Upon nanoparticle dissociation inside of cancer tissue, SiNc with hydrophobic axial substituents may be capable of regaining intermolecular repulsion in order to recover NIR fluorescence.

To test our theory, silicon 2,3-naphthalocyanine bis(trihexylsilyloxide), a SiNc molecule modified with two trihexylsilyloxide substituents was employed (Figure 1). There are two main reasons for choosing the trihexylsilyloxide ligand. First, compared to other available SiNc derivatives, such as those with dihydroxide or dichloride substituents, the relatively long alkyl chains contribute additional hydrophobicity to the molecule (water solubility <1 ng/mL), which facilitates polymeric nanoparticle

encapsulation and minimizes leaching of SiNc from nanoparticles in an aqueous environment [35]. More importantly, the high hydrophobicity may enable sufficiently dense SiNc packing within the nanoparticle's hydrophobic core, potentially to the maximum spatial allowance of a polymeric nanoparticle. This in turn would drive SiNc molecules to a close proximity for self-quenching and the turning off of NIR fluorescence. Secondly, the bulky ligands can afford steric protection to prevent permanent self-aggregation of SiNc molecules during nanoparticle fabrication and after release from the nanoparticles.

We prepared three SiNc-PNP formulations by fixing the polymer PEG-PCL concentration (10 mg/mL) but varying SiNc concentrations of 0.05, 0.30, and 0.60 mg/mL in the solutions. The nanoparticles loaded with different amounts of SiNc (0.5%, 3%, and 6% SiNc/polymer loading efficiency) were synthesized via a water addition/solvent evaporation method. The actual encapsulated SiNc concentrations were quantified and confirmed by NIR absorbance measurements. NIR fluorescence intensity (F.I.) of the three nanoparticles was then compared by measuring solutions diluted to the same SiNc concentration at 0.01 mg/mL. As seen in Figure 2A, the NIR fluorescence of SiNc-PNP was indeed dependent on the SiNc loading concentration. The PNPs with the lowest SiNc loading (0.5% SiNc/polymer) displayed the highest F.I. (quantum yield ~11.8%), and the F.I. decreased with increasing SiNc payload. The PNPs with the highest SiNc loading (6% SiNc/polymer) exhibited no fluorescence. We used the Pearl Imaging Systems to record NIR fluorescence images of the three SiNc-PNP solutions and the images were consistent with F.I. measurements, with 0.5% SiNc loading exhibiting the brightest fluorescence and 6% SiNc loading showing no fluorescence (Figure 2A). Therefore, we selected the 6% SiNc payload to construct our activatable SiNc polymeric nanoparticles.
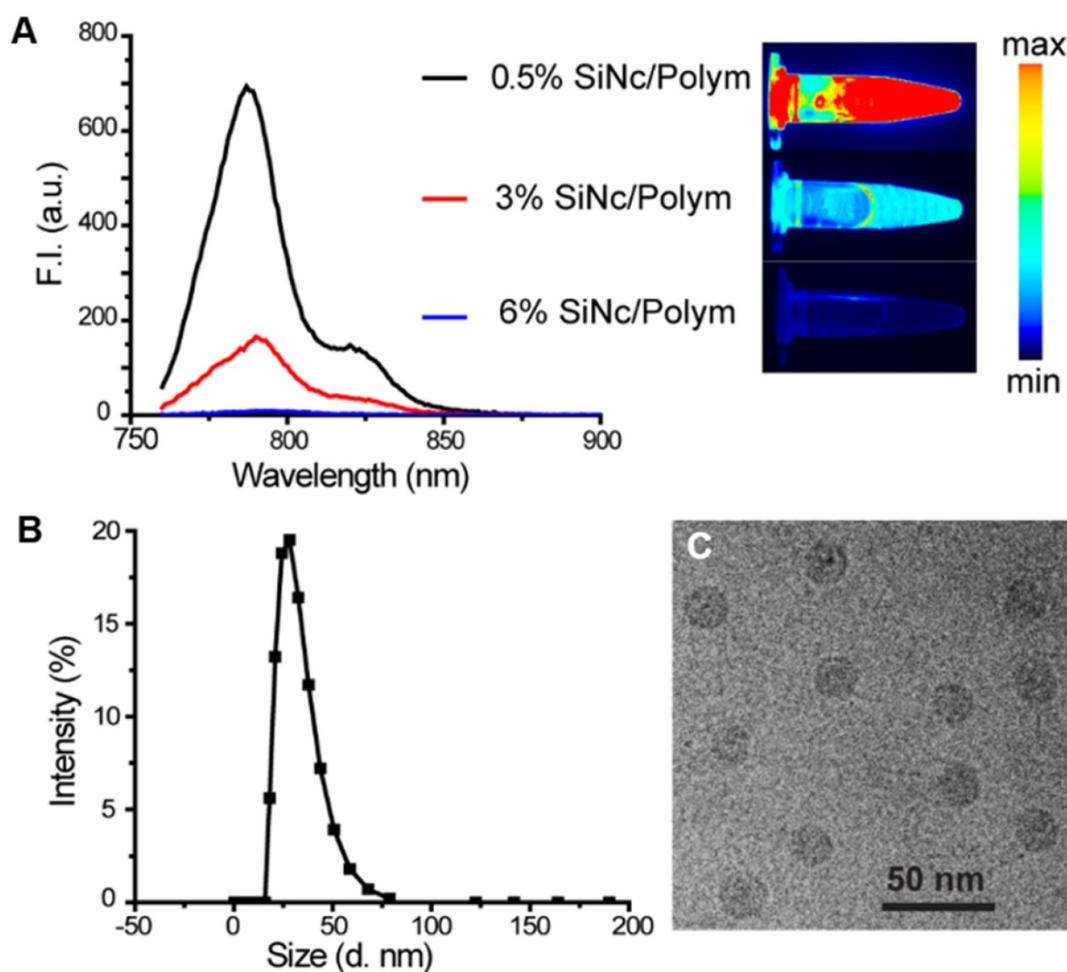

Figure 2. (**A**) Fluorescence spectrum (λ_{ex} = 750 nm) and corresponding NIR images of SiNc-PNPs aqueous solutions made with different SiNc loading amounts (0.5%, 3%, and 6% based on Equation 1 in Supplementary Material). Fluorescence of all three NPs was measured at the same SiNc concentration of 0.01 mg/mL. NIR images were collected by the Pearl Impulse Small Animal Imaging System. (**B**) Size profiles of the developed nanoparticles tested by DLS. (**C**) Representative cryoTEM image of SiNc-PNPs (6% SiNc/polymer loading). Scale bar is 50 nm.

Of note, the only difference between the herein reported always-ON and activatable nanoplatforms is in the amount of dye (SiNc) loaded into the PEG-PCL nanoparticles. By increasing the amount of SiNc inside the hydrophobic core of PEG-PCL nanoparticles, we anticipated that SiNc molecules would pack closely and the distance between them would significantly decrease, thereby promoting the self-quenching effect and resulting in negligible fluorescence emission. By evaluating the absorption spectra, we observed that always-ON nanoparticles loaded with the lowest amount of SiNc (0.5% SiNc/polymer) exhibited an absorbance peak at 784 nm, which was red shifted by 5 nm from the Q-band maximum at 779 nm of monomeric non-encapsulated SiNc dissolved in THF (Figure S1). Furthermore, the absorbance maximum of activatable nanoparticles loaded with the highest amount of SiNc (6% SiNc/polymer) was red shifted by 10 nm from the Q-band maximum of monomeric SiNc (Figure S1). Katayose et al. previously revealed that packed SiNc molecules with axial substituents exhibit a red shift of Q-band absorption and the red-shift value is mainly dependent on the center-to-center distance between molecules [40]. It was also demonstrated that the red-shift value increases with a decrease in the distance between SiNc molecules. Therefore, we can speculate that by increasing the amount of SiNc inside the PEG-PCL nanoparticles, the distance between the SiNc molecules decreased, thereby causing energy transfer among molecules and fluorescence self-quenching. Petrásek et al. previously evaluated the concentration-dependent quenching of phthalocyanine derivatives and the calculated value of the critical distance for energy transfer between molecules was 5.98 nm [41].

The developed activatable SiNc-PNPs featured an average hydrodynamic diameter of ~40 nm and a monodisperse size distribution, as indicated by DLS analysis (Figure 2B) with a polydispersity index (PDI) of 0.092 ± 0.005. Cryo-TEM studies further confirmed the preparation of monodisperse spherical nanoparticles (Figure 2C). As we previously reported, the always-ON SiNc-PNPs have a very similar hydrodynamic diameter and size distribution [35].

In Vitro evaluation of activatable SiNc-PNP

As predicted above, the employed SiNc is a highly hydrophobic molecule and therefore its leaching from the lipophilic core of the developed PNP in an aqueous environment, including human plasma, was negligible (Figure 3A). Thus, SiNc demonstrates minimal release when compared, for instance, to the ICG's hydrophobic analog, IR775, loaded into the same PEG-PCL nanoparticle (Figure

3B) [30, 35]. This is most probably related to the fact that SiNc has substantially lower water solubility (<1 ng/mL) than IR775 (2.3 μg/mL). Consequently, this intrinsic property of SiNc molecules can minimize their leaching from the nanoparticles in systemic circulation, thus diminishing the background signal from released fluorophores.
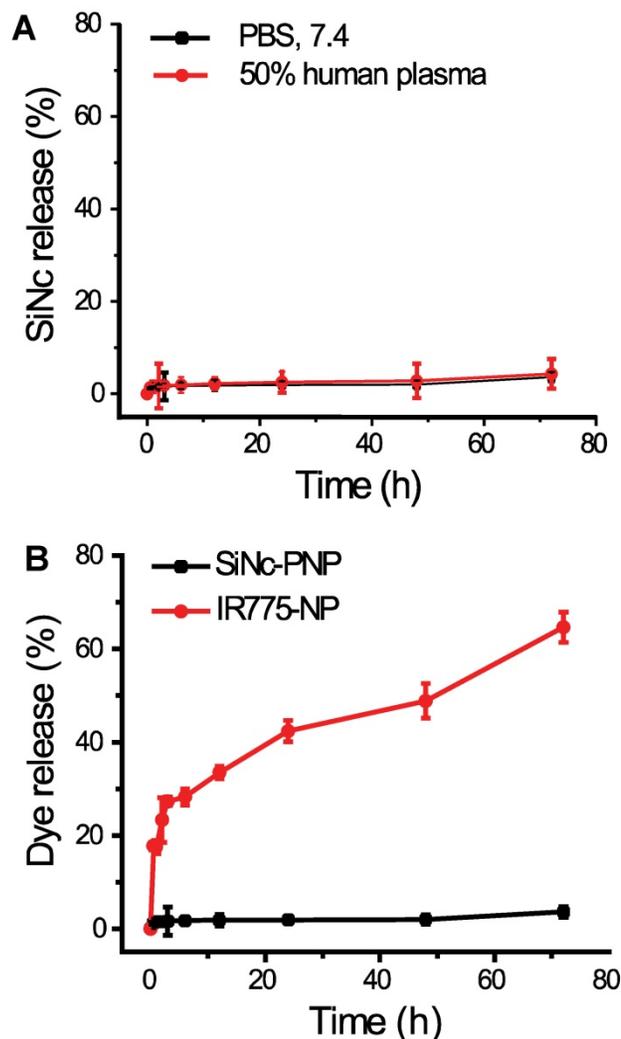

Figure 3. (**A**) The release profiles of SiNc from SiNc-PNP incubated at 37 °C in 50% human plasma and PBS buffer at pH 7.4. (**B**) The release profiles of SiNc and IR775 from PEG-PCL nanoparticle incubated at 37 °C in PBS buffer at pH 7.4.

To investigate whether the developed SiNc-PNP can be internalized into cancer cells and activate their fluorescence, cell studies were performed prior to animal experiments. PEG-PCL was labeled with fluorescein isothiocyanate (FITC) at the distal end of PEG for tracking the polymer component of the activatable SiNc-PNP, while the intrinsic fluorescence of SiNc was employed for tracking the dye. FITC-labelled activatable SiNc-PNP were prepared using 1% w/w of FITC-PEG-PCL mixed with

non-modified PEG-PCL. Nanoparticles were incubated with human ovarian cancer cells A2780/CDDP in cell culture medium with 10% bovine serum for different periods of time. At each time point, both cells and culture medium were imaged for FITC and SiNc (Figure 4). After 0.5 h, FITC fluorescence was found inside cells and culture medium while no NIR fluorescence generated by SiNc could be observed, indicating that cellular uptake of nanoparticles occurred in a timely manner, within 0.5 h, and nanoparticles remained intact and non-fluorescent before intracellular internalization (Figure S2).

After 4 h, the appearance of SiNc fluorescence was detected inside the cells, but not in the medium, and the NIR fluorescence was mostly overlapped with FITC fluorescence. As time went on, more SiNc fluorescence was observed inside the cells after a 24 h incubation period, and microscopy images revealed SiNc fluorescence partially overlapped with FITC fluorescence at this time point. This may indicate SiNc diffusion from the polymeric carrier. Of note, SiNc fluorescence was not detected in cell culture medium at the studied time points, revealing that SiNc was not released prior to intracellular internalization (Figure S2). This fact was also confirmed by incubating the activatable SiNc-PNP in human plasma at 37° C, demonstrating no recovered fluorescence even after 48 h (Figure S3).

Based on the obtained results, we can conclude that the activation of SiNc fluorescence primarily occurred following SiNc-PNP internalization into cancer cells (Figure 4), but not in human plasma (Figure S3) or serum containing cell medium (Figure S2). This suggests that the complex intracellular environment is capable of compromising the integrity of self-assembled PEG-PCL nanoparticles. Consequently, SiNc can be released and therefore tight packing of quenched SiNc molecules in the hydrophobic core of the nanoparticles is disrupted. These alterations result in switching the quenched SiNc molecules to the ON fluorescence state. The proposed mechanism of SiNc activation is in good agreement with the previous studies that reported activatable polymeric nanoparticles and micelles containing quenched fluorophores in their hydrophobic cores [33, 42]. For example, to develop fluorescence activatable nanoparticles, Lee et al. chemically conjugated hydrophobic PpIX fluorophore to hydrophilic glycol chitosan (GC) polymer [42]. The synthesized amphiphilic conjugates can self-assemble in aqueous solution to form stable nanoparticles and PpIX fluorophores exhibited self-quenching due to their tight packing in the hydrophobic core. After internalization into cancer cells, the behavior of these

nanoparticles was very similar to our activatable SiNc-PNP (Figure 4). At 10 min post-incubation, the green fluorescence of FITC-labeled GC polymer was distributed throughout the cytoplasm; however, the fluorophores did not present any red fluorescence signal due to the self-quenching effect of PpIX molecules in the nanoparticles. As time went on, the red fluorescence intensity of PpIX fluorophores started to appear in the cells, indicating that PpIX fluorescence was restored to the ON state. Therefore, it was concluded that the intracellular environment gradually undermines the integrity of the nanoparticle's structure, thereby disrupting the dense packing of PpIX fluorophores in hydrophobic cores and restoring PpIX fluorescence. Along with *in vitro* studies, Lee et al. also tested the changes in the integrity of the nanoparticles in the presence of a surfactant such as 5 wt% sodium dodecyl sulfate (SDS). Based on the previous reports it was assumed that surfactants disrupt the highly dense hydrophobic cores of self-assembled nanoparticles, and this phenomenon similarly occurred by intracellular proteins in the cell cytosol [33, 42, 43]. As expected, the size and distribution of the PpIX-loaded nanoparticles changed significantly, indicating that the surfactant disrupts the highly dense PpIX hydrophobic cores in the nanoparticles. Consequently, the dramatic increase in the fluorescence intensity was detected in the aqueous solution. The same experimental strategy was employed by another team to characterize self-quenchable ICG-encapsulated micelles that become fluorescent in the intracellular environment [33]. Therefore, we also tested our nanoparticles in the presence of a surfactant and a similar behavior was observed. DLS and TEM studies revealed that the size of the nanoparticles significantly decreased (Figure 5A and B), indicating their disintegration. In addition, strong fluorescence signal was detected in the water solution of activatable SiNc-PNP (Figure 5C). This result reveals that SDS also behaves as a dispersion agent for the released SiNc molecules.

In a separate experiment, we determined that an acidic environment (pH = 6.5-4.5) can also contribute to the activation of SiNc-PNP fluorescence by compromising the integrity of self-assembled SiNc-loaded PEG-PCL nanoparticles and thereby inducing SiNc release from the hydrophobic core. The activatable SiNc-PNP demonstrated a significant increase in dye release when incubated at 37°C at pH lower than 7.4 (Figure 5D), such as pH 6.5 (~40% dye release) and pH 4.5 (~60% dye release). Simultaneously, DLS measurements revealed that particles size and distribution changed upon decreasing pH (Figure 5E and F), which might

indicate distortion of nanoparticle structures. The TEM images also demonstrated that there is a fraction of nanoparticles with larger size at lower pH (Figure 5 G, H, and I). Of note, it is challenging to demonstrate the activation of SiNc fluorescence under lower pH in aqueous solution. This can be related to the fact that SiNc has negligible water solubility (<1 ng/mL) and, therefore, the dye molecules released from the hydrophobic core can aggregate and precipitate in aqueous solution. The precipitation of SiNc was detected by visual inspection of a vial containing SiNc-PNP solution under lower pH. Moreover, we observed that the absorption intensity of SiNc-PNP solution significantly decreased following 24 h incubation at the lower pH, indicating SiNc release and precipitation (Figure S4a). As a result, our measurements revealed only minimal increase in fluorescence intensity of SiNc-PNP solution with lower pH due to the above described observations (Figure S4b).

The results obtained under acidic pH support our proposed mechanism of SiNc activation because PEG-PCL nanoparticles are usually internalized inside cancer cells by endocytosis [44] and, therefore, disintegration of some nanoparticles and release of SiNc can occur inside the endosome/lysosome (pH 4.5-6.5) of tumor cells [45]. In addition, the acidic environment of solid tumors (pH = 6.5-6.8) can also trigger the release of SiNc from the developed nanoparticles [46].

Because fluorescence of the developed SiNc-PNP is activated in cancer cells, one would expect that these nanoparticles might also disintegrate and generate fluorescence following internalization into non-malignant cells. To clarify this possibility, we treated HEK293 kidney cells with FITC-labeled SiNc-PNP under the same experimental conditions. The flow cytometry data indicated that the internalization efficiency of SiNc-PNP into HEK293 cells was very low and <8% of cells generated green fluorescence 24 h after incubation with FITC-labeled SiNc-PNP (Figure S5).
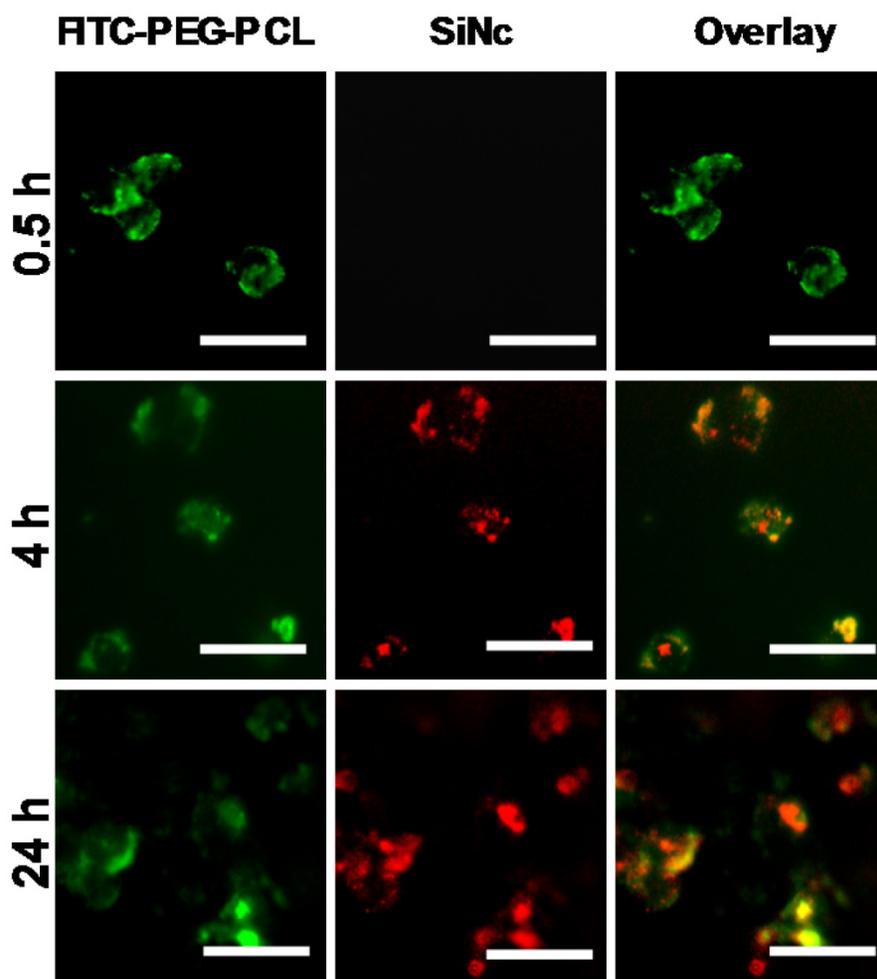

Figure 4. Representative fluorescence microscopy images of A2780/CDDP ovarian cancer cells at different incubation periods (0.5, 4, and 24 h) with activatable SiNc-PNP prepared with FITC-labelled PEG-PCL. The left panel shows images of A2780/CDDP ovarian cancer cells obtained at Ex. 470/Em. 510 nm, representing fluorescence signals from FITC-PEG-PCL; the middle panel show images obtained at Ex. 710/Em. 775 nm, representing NIR fluorescence signals from SiNc; the right panel is an overlay of the first two panels. All images were acquired using a 40 × objective; scale bar is 50 μm for all images.
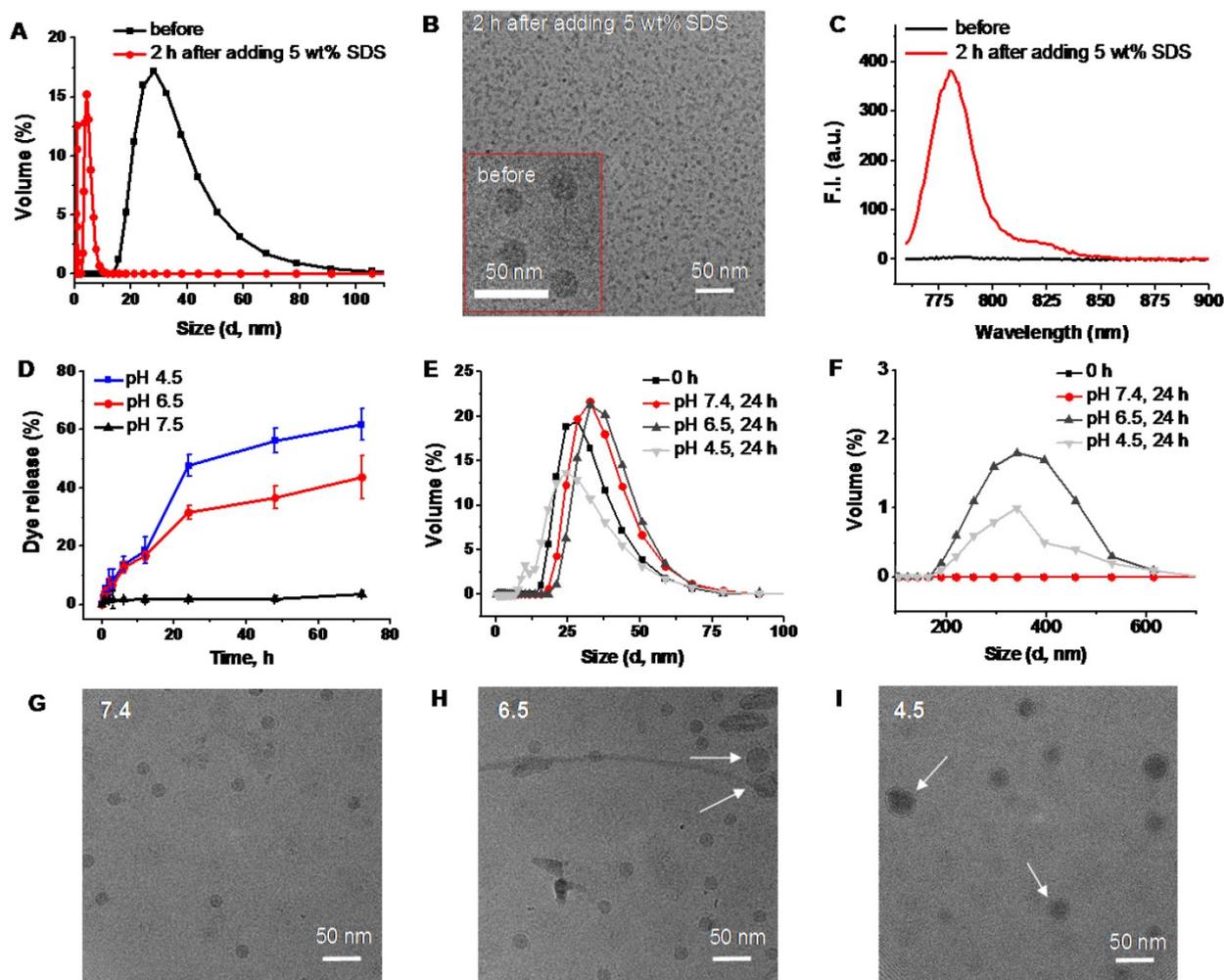
Figure 5. DLS size profiles (**A**), representative cryoTEM images (**B**), and fluorescence spectra (**C**) of SiNc-PNPs before and after incubation for 2 h in PBS buffer with 5 wt% SDS. (**D**) The release profiles of SiNc from activatable SiNc-PNP incubated at 37 °C in PBS buffer at pH 7.4, 6.5 and 4.5. DLS size profiles of the developed activatable SiNc-PNP after incubation at 37 °C for 24 h in PBS buffer at pH 7.4, 6.5 and 4.5 in the 0-100 nm (**E**) and 100-700 nm (**F**) ranges. Representative cryoTEM images of the developed activatable SiNc-PNP after incubation at 37 °C for 24 h in PBS buffer at pH 7.4 (**G**), 6.5 (**H**) and 4.5 (**I**). Presence of bigger nanoparticles at lower pH is indicated by arrows.

In addition, fluorescence microscopy analysis of the selected kidney cells that were transfected with FITC-labeled SiNc-PNP revealed that only negligible SiNc fluorescence signal appeared after 24 h of incubation (Figure S6). Similar behaviors of nanoparticles, including micelles, has been previously reported [47, 48]. For example, by performing *in vitro* tests on co-cultures of cancer and normal breast cells, Mauro et al. demonstrated that self-assembled micelles were selectively internalized into the cancer rather than normal cells [48]. The observed differences between malignant and normal cells could be related to the fact that PEG-PCL-based nanoparticles exploit the process of endocytosis to gain entry inside cells [44]. These pathways are generally upregulated in cancer cells to ensure large amounts of extracellular proteins are internalized and catabolized by the endo/lysosomal system, providing a constant supply of nutrients to rapidly dividing cancer cells [49].

Therefore, aberrations in the endocytosis processes lead to differential uptake of nanoparticles inside cancer cells when compared to normal cells [50-52]. Our *in vivo* studies further confirmed the obtained *in vitro* results. Figure 6 demonstrates that in contrast to the cancer tumor, only negligible fluorescence was detected in healthy organs of mice treated with the activatable SiNc-PNP.

In Vivo evaluation of the activatable SiNc-PNP

To further validate our activatable nanoparticles for *in vivo* cancer imaging, mice with subcutaneous ovarian cancer tumors were used for evaluation of their tumor targeting and organ distribution. Activatable (OFF/ON SiNc-PNPs) and always-ON nanoparticles (SiNc-PNPs, SiNc loading concentration = 3% SiNc/polymer, see Figure 2A) were administrated intravenously (i.v.) into mice, and *in vivo* NIR fluorescence images were collected using a

Pearl Impulse Small Animal Imaging System at different time points. The obtained data revealed that no fluorescence was observed 2 h post-injection of activatable SiNc-PNPs (Figure 6A), whereas fluorescence was generally found spread over the whole mouse body within the same period of time when using the always-ON imaging agent (Figure 6A) [27, 35]. At 10 h post-injection, NIR fluorescence could be detected at the tumor site, indicating accumulation of activatable SiNc-PNP as well as release and fluorescence recovery of SiNc from polymeric nanoparticles (Figure 6A). After 24 h, strong fluorescence was observed within the tumor with high tumor-to-normal tissue contrast for sensitive fluorescence detection, revealing the significant accumulation of fluorescence-recovered SiNc. To further assess the distribution of both activatable and always-ON SiNc-PNPs, tumors and various organs (liver, kidneys, spleen, heart, and lungs) were collected and imaged 24 h after injection. The

obtained images revealed enhanced fluorescence signal in cancer tumors, demonstrating an effective accumulation of both activatable and always-ON nanoparticles in malignant tissues (Figure 6B). The prepared nanoparticles have the required features such as ~40 nm hydrodynamic size, slightly negative zeta potential (-2.8 mV) and PEGylated surface, which ensure efficient passive cancer targeting. To further confirm efficient accumulation of SiNc-loaded PEG-PCL nanoparticles, we compared the NIR fluorescence distributions in organs and tumors 24 h after i.v. injection of activatable and always-ON SiNc-PNP in mice with intraperitoneal xenografts of human ovarian cancer (Figure S7). By quantifying the distribution of NIR fluorescence in various organs, we demonstrated that ~35% of total fluorescence generated by the always-ON SiNc-NP was detected in cancer tumors 24 h after intravenous injection (data not shown).
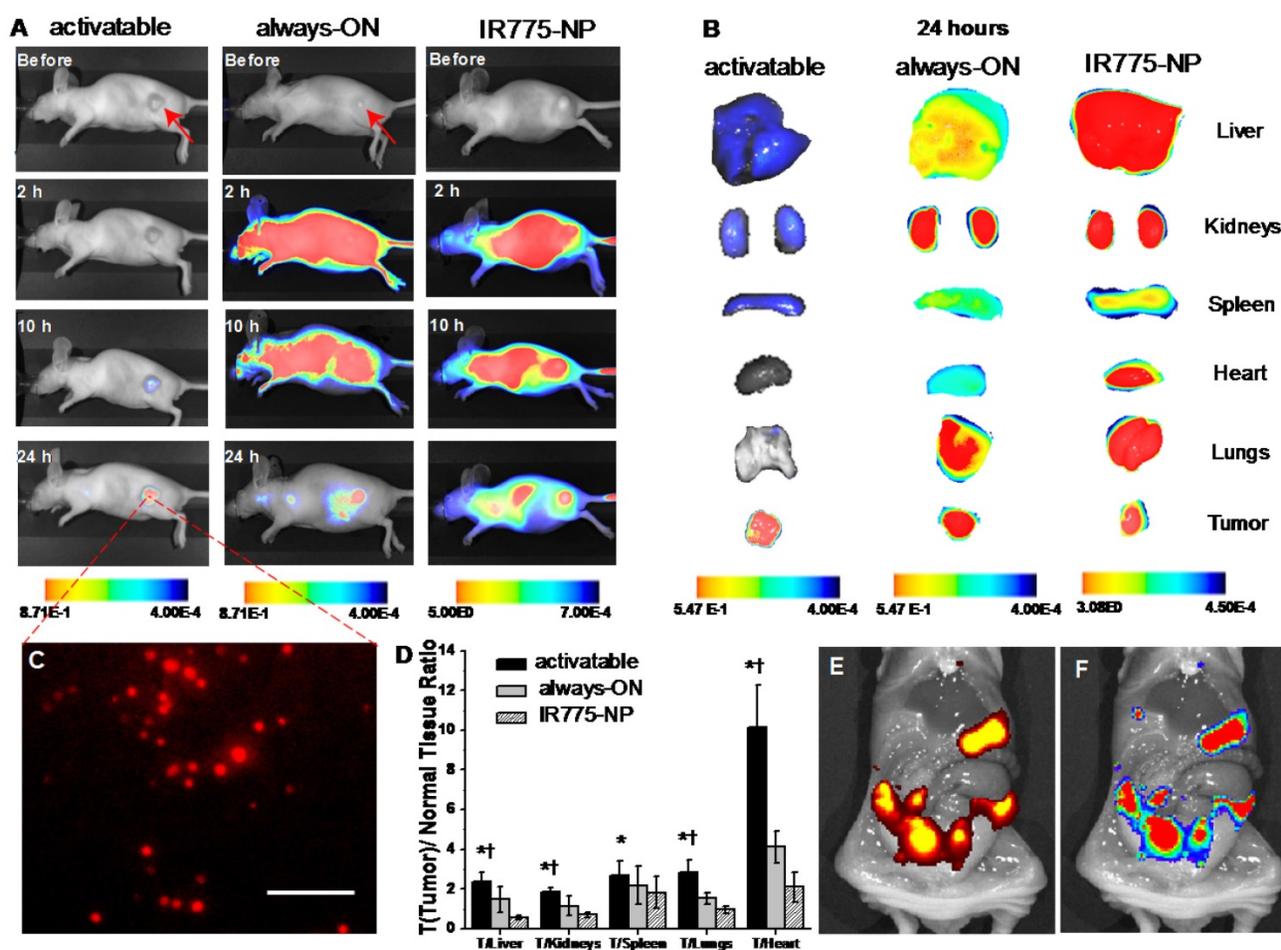

Figure 6. Biodistribution and NIR fluorescence recovery of SiNc-PNPs in nude mice and tumors. (**A**) Fluorescence images of the nude mice with subcutaneous cancer tumors before and 2, 10, and 24 h after i.v. administration of activatable and always-ON SiNc-PNP and compared to IR775-NP. (**B**) Fluorescence images of various organs and tumors were acquired at 24 h post-injection. (**C**) Fluorescence image of tumor cross-section (the core of the 300 mm³ tumor). Scale bar is 100 µm. (**D**) Tumor-to-normal tissue (T/N) analysis of fluorescence intensity in subcutaneous tumors and organs harvested from mice 24 h after injection with IR775-NP, activatable and always-ON nanoparticles. *$P < 0.05$ when activatable nanoparticles are compared with always-ON nanoparticles. †$P < 0.05$ when activatable nanoparticles are compared with IR775-NP. Distribution of (**E**) bioluminescence and (**F**) SiNc-generated NIR fluorescence in the abdominal cavity 24 h after i.p. injection of activatable SiNc-PNP into mice with intraperitoneal xenograft of luciferase-labeled ES2 ovarian cancer cells. *Note:* only cancer tissues generate bioluminescence signal in D-luciferin-injected animals.

It is worth noting that strong fluorescence signal was also detected in the liver, kidneys, spleen and lungs 24 h post-injection of the always-ON nanoparticles (Figure 6B and S7). In contrast, only dim fluorescence was displayed in the liver, kidneys, and spleen 24 h following systemic administration of activatable nanoparticles, indicating that SiNc molecules were predominantly released in cancerous tumors and, therefore, provide high tumor-to-normal tissue contrast for sensitive fluorescence imaging (Figure 6A, B and S7).

To quantitatively evaluate the efficiency of the activatable nanoparticles in comparison to the previously published always-ON nanoparticles, we calculated tumor-to-normal tissue (T/N) ratios in mice injected with each formulation. The T/N ratio is defined as the ratio between the fluorescence signal in the region of interest within the tumor, and the fluorescence signal in the region of interest within the normal tissues including kidneys, liver, and lungs. When compared to mice treated with always-ON nanoparticles, the T/N ratios in liver (tumor/liver ratio), kidney (tumor/kidney ratio), and lungs (tumor/lungs ratio) of mice injected with the activatable nanoparticles increased 1.6-, 1.6- and 1.9-fold, respectively (Figure 6D). In addition, similar changes in the T/N ratios were observed when mice with intraperitoneal xenografts of human ovarian cancer were i.v. injected with both formulations (Figure S7). These results suggest that the activatable nanoparticles have the higher potential for differentiating tumor and normal tissue during image-guided surgery.

The turning-on behavior of the developed nanoparticles in the animal studies was in agreement with the *in vitro* studies (Figures 4 and S2). Nanoparticles were stable and remained non-fluorescent in the bloodstream until they reached and accumulated at the tumor, and in a few hours SiNc-PNP fluorescence was activated predominately at the cancerous tissue. It should be taken into consideration that the fluorescence recovery rate could differ *in vitro* and *in vivo*, due to the possibility of different release and degradation rates of PEG-PCL in different environments [53, 54].

It is also important to emphasize that SiNc's structure plays a crucial role in the development of tumor activatable fluorescence nanoparticles for selective tumor imaging. When the biodistributions of the studied activatable and always-ON SiNc-loaded nanoparticles were compared to that of the hydrophobic ICG analog, IR775, loaded into the same PEG-PCL nanoparticle, we observed lower tumor selectivity and higher accumulation in other organs after 24 h (Figure 6A, B and D). This might be related

to the fact that IR775 has higher aqueous solubility (2.3 µg/mL) than SiNc (< 1 ng/mL). Therefore, it could leach from nanoparticles in an aqueous environment (Figure 3B) including systemic circulation and non-specifically accumulate in healthy organs (Figure 6). Moreover, the released hydrophobic IR775 molecules could demonstrate slow clearance from the body, as evidenced by the strong fluorescence signal in various organs 24 h after injection. To test our assumption, aqueous solution of the free IR775 dye containing 5% DMSO was i.v. injected into mice bearing subcutaneous xenografts of ovarian cancer. *In vivo* fluorescence measurements revealed strong fluorescence signal in all organs at 24 h following injection (Figure S8), confirming the slow clearance of the hydrophobic IR775 from the body. In contrast, SiNc has negligible aqueous solubility (<1 ng/mL) [35] and therefore demonstrated minimal release from nanoparticles (Figure 3A and S2) as well as decreased accumulation in healthy organs (Figure 6).

For the purpose of intraoperative imaging as well as combined phototherapy, it is crucial to ensure tumor penetration of the imaging and therapeutic agents, as opposed to just superficial tumor accumulation. A tumor with a size of 300 mm^3 was excised 24 h post i.v. injection of activatable SiNc-PNP and was then used for paraffin tissue embedding. Slices were sectioned from the core of the embedded tumors and were examined using fluorescence microscopy. Figure 6C exhibits significant NIR fluorescence emitted from SiNc, confirming infiltration of SiNc into the core of the solid tumor.

Next, we also validated the high tumor targeting capability of the developed activatable SiNc-PNP into mice with intraperitoneal xenografts of human ovarian cancer. This model simulates the process of peritoneal dissemination in intra-abdominal cancers such as ovarian cancer [55]. The mice were inoculated with luciferase-expressing ES-2 (ES-2/Luc) cells and monitored intraperitoneally (i.p.) for cancer formation and progression as well as identification of cancerous tumors. The activatable SiNc-PNP dosage was the same as that in the subcutaneous model studies. Mice were injected with D-luciferin 10 min prior to imaging; the IVIS imaging system was used to monitor bioluminescence representing tumor growth as well as NIR fluorescence from SiNc. Figures 6E and F show the bioluminescence and NIR fluorescence images of a mouse abdominal cavity 24 h after i.p. injection of activatable SiNc-PNP, revealing a strong overlap between bioluminescence and fluorescence signals generated by luciferase-transfected cancer cells and SiNc, respectively. In addition, two administration routes, i.p. and i.v. injection, of

activatable SiNc-PNP were examined and compared for probe delivery and target efficacy. Despite the administration route difference, all tumors in both cases were targeted and labeled with fluorescence generated by SiNc (Figure S9).

The positive results of the *in vivo* evaluation of the activatable nanoparticles as a tumor-activated NIR imaging agent encouraged us to assess their intraoperative imaging feasibility. In the next step, we explored tumor debulking with the aid of the activatable SiNc-PNP using an FDA-approved intraoperative imaging system, Fluobeam® 800. Real-time videos were recorded during the surgical removal of a subcutaneous A2780/CDDP xenograft tumor from a mouse 24 h after i.v. injection of activatable SiNc-PNP (3.0 mg/kg SiNc). During the operation, the tumor was successfully removed with the guidance of the strong NIR signal from SiNc detected and displayed on a monitor (a real-time surgery video is available, please see Supplementary Video: Surgery 1). Figures 7A, B and C give representative images isolated from the recorded video, showing bright NIR fluorescence detected at the tumor site before resection, after incision, and after complete resection. These raw images are a real-time reflection of the visual readout during the image-guided operation and revealed high cancer-to-normal tissue contrast. Additionally, the intensity of the signal generated by SiNc was stable without any visible alteration during the entire time of the surgery, confirming the high photostability possessed by SiNc.

Finally, efficiency of fluorescence image-guided surgery mediated by this nanoplatform was validated in mice with intraperitoneal xenografts of human ovarian cancer. After resection of the visible tumor mass we demonstrated that real-time activatable SiNc-PNP-mediated image-guided surgery provided successful detection of a 2 mm tumor in a mouse abdominal cavity (Figure 7D, a real-time surgery video is available, please see Supplementary Video: Surgery 2). The compatibility with the Fluobeam® emphasizes the promising potential of activatable SiNc-PNP as an intraoperative imaging agent, substantially lowering barriers to clinical translation of our nanoplatforms.

In Vivo antitumor efficiency of the activatable SiNc-PNP

The effective phototherapeutic properties of the always-ON SiNc-PNP were confirmed earlier *in vitro* and *in vivo* [35]. To confirm the phototherapy effect *in vitro* for the activatable SiNc-PNP, the A2780/CDDP were treated with different concentrations (20 and 50 µg/mL) of the activatable SiNc-PNP followed by

formation of cell pellets 24 h post treatment. The treated cell pellets were exposed to the 10 min NIR irradiation and demonstrated concentration dependent cell eradication. The temperature within the 50 µg/mL treated cell pellet reached ~50 °C, demonstrating *in vitro* heat generation (photothermal therapy mechanism, Figure S10a) as well reactive oxygen species (ROS) formation (photodynamic therapy mechanism, Figure S10b). The antitumor efficiency of phototherapy mediated by activatable SiNc-PNP was assessed *in vivo* using a murine xenograft model established by subcutaneous inoculation of A2780/CDDP cells. The choice of the mouse model with the subcutaneous xenograft was dictated by the fact that the direct irradiation of the cancer tumor with NIR light is required for the phototherapy. The selected model allowed us to efficiently evaluate the proposed phototherapy for treatment of platinum-resistant human ovarian cancer while avoiding stress to the mice associated with an incision of the abdominal wall for delivering NIR light to the intraperitoneal xenograft.

When the tumor volume reached ~75 mm^3, the activatable SiNc-PNP was administrated i.v. into mice by a single dose, and NIR treatment was implemented 24 h post administration (OFF/ON SiNc-PNP NIR) at the highest nanoparticle accumulation as determined by biodistribution studies. Mice injected with saline followed by NIR treatment (Saline NIR), as well as mice injected with activatable SiNc-PNP (OFF/ON SiNc-PNP) or saline without NIR treatment (Saline) were used as different control groups. The extent of tumor growth was then closely monitored and documented (Figure 8A). Tumors in the saline alone group progressed aggressively, approaching the humane endpoint within 16 days. Likewise, tumors in the saline with NIR treatment group advanced rapidly as well, confirming that the NIR laser exposure alone had no therapeutic effect. The activatable (OFF/ON) SiNc-PNP alone did not impact tumor growth, with similarly aggressive tumor progression as the Saline and Saline NIR groups. However, tumors in the activatable SiNc-PNP with NIR treatment group were eradicated by day 2-4 after administration with a 10 min laser exposure (Figure 8A), and no tumor recurrence was observed for 27 days post phototherapy treatment.

Of note, the mice used for phototherapy studies (Figure 8) were not treated with any surgery, including image-guided surgery. The developed combinatorial phototherapy is an adjuvant intraoperative treatment and its main goal is to eliminate tumors that may be left behind or are challenging to resect without damaging healthy organs. If complete resection of the turn-on

fluorescent tumors is achieved, the phototherapy will not be required. To evaluate the full potential of this therapy we, therefore, tested it on cancer tumors that were not exposed to surgical resection.

The intratumoral temperature was measured as a means to estimate activatable SiNc-PNP's phototherapeutic activity. Figure 8B revealed that the intratumoral temperature rose from 34 °C to 55 °C during the SiNc-PNP-mediated phototherapy, whereas temperature was maintained within 1 °C in the control mouse. The temperature change was achieved at 785 nm wavelength with 1.3 W/cm^2 laser power density, and it was sufficient to ablate malignant tissues. Slight skin burns were observed in the activatable SiNc-PNP with NIR treatment group, suggesting significant heat generation of abundant SiNc delivered to cancerous tissues. However, the burns were all healed after applying an antibiotic ointment (Figure S11). To confirm sufficient tissue penetration of the employed NIR light, we validated in a separate experiment that heat can be efficiently generated by the activatable SiNc-PNP deep within tumors, up to 12 mm from the point of NIR light (1.3 W/cm^2) application (Figure S12).

To prevent phototherapy burn, we investigated the tunability of the photothermal response by controlling the NIR laser power. Our results revealed that the intratumoral temperature change was dictated by the laser power, which demonstrated the fine regulation of phototherapy administration provided by the developed nanoplatforms. Our studies further revealed that, when laser power density is lowered from 1.3 W/cm^2 to 0.5 W/cm^2, the activatable (OFF/ON) SiNc-PNPs are not capable of heat generation (Figure S13). This fact has clinical significance. Intraoperative imaging systems (e.g. FLARE™, Fluobeam 800) use an excitation power density less than 0.025 W/cm^2 [9, 14], which is not high enough to induce heat via activatable SiNc-PNPs. Thus, phototherapy would not happen spontaneously during image-guided surgery, and treatment could be customized by using a NIR light of the desired power (> 0.5 W/cm^2, Figure S13).

Of note, two separate groups of mice were used for evaluation of phototherapy efficacy and intratumoral temperature. To measure intratumoral temperature, a fiber optic temperature probe was inserted into a tumor through an 18-gauge needle. With needle insertion, tumor tissue disruption occurred and it can potentially influence the tumor growth. To avoid this effect and properly evaluate the efficacy of phototherapy, the separate group of mice was employed for the measurement of intratumoral temperature. The purpose of Figure 8b is only to demonstrate that the temperature change in a tumor was achieved with NIR light exposure, and it was sufficient to ablate malignant tissues. Of note, in our previous report [35] we demonstrated that SiNc-PNP in combination with NIR can maintain constant intratumoral temperature as long as the NIR laser is on.
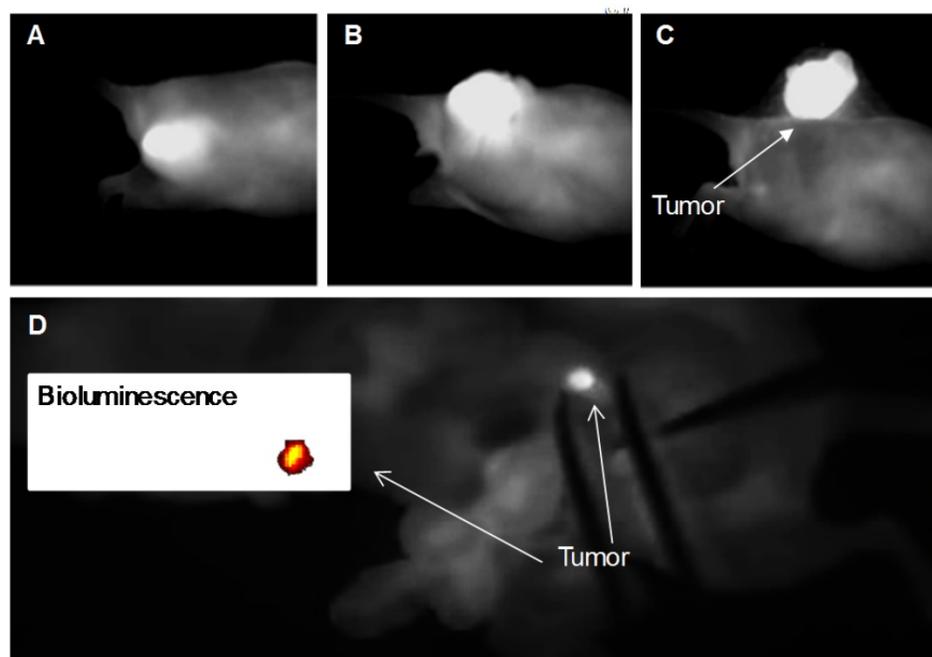

Figure 7. NIR fluorescence images recorded with Fluobeam® 800 during the activatable SiNc-PNP-guided intraoperative tumor resection at various time points: (**A**) before resection, (**B**) after incision, and (**C**) complete resection of the tumor. The mouse bearing a A2780/CDDP xenograft was injected i.v. with activatable SiNc-PNP (3.0 mg/kg SiNc) 24 h before surgical resection. (**D**) NIR fluorescence image of a mouse abdominal cavity recorded with Fluobeam® 800 during SiNc-PNP-guided surgery. Inset represents the bioluminescence image of the identified and resected cancer tissue (2 mm in size). The mouse with ES2 was injected i.v. with activatable SiNc-PNP 24 h before surgical resection.

Despite the strong anticancer effect of combinatorial phototherapy (Figure 8), the mice did not lose body weight or display any signs of toxicity (e.g., appearance, behavior) after the injection of the activatable SiNc-PNP. As shown in Figure 9A, mice from all four groups featured similar body weight patterns, showing no adverse effects from treatment with activatable SiNc-PNP nor NIR.
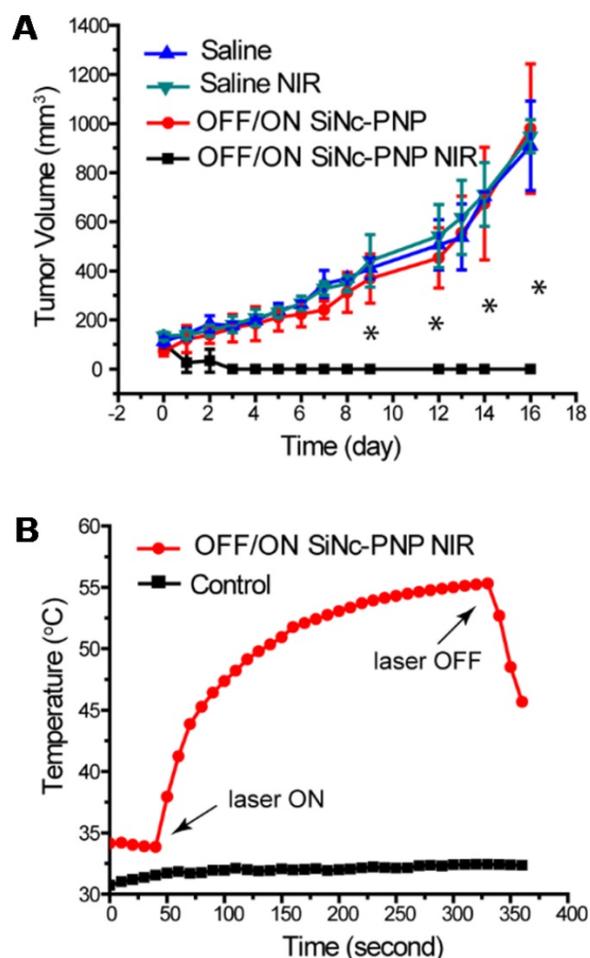

Figure 8. Phototherapy outcomes in nude mice with A2780/CDDP subcutaneous xenografts after single dose injection of activatable (OFF/ON) SiNc-PNP (3 mg/kg of SiNc). (**A**) Tumor growth profiles after i.v. injection of OFF/ON SiNc-PNP with (black curve) or without (red curve) NIR light exposure for 10 min (785 nm, 1.3 W/cm2) as well as after i.v. injection of saline with (green curve) or without (blue curve) NIR light exposure for 10 min (785 nm, 1.3 W/cm2). Mice were injected 24 h prior to NIR irradiation treatment, which was performed on Day 0. (**B**) Temperature profile inside of cancer tumors record during the NIR phototherapy mediated by the OFF/ON SiNc-PNP (3 mg/kg of SiNc) one day post-injection (red curve). Tumors exposed to NIR light with injection of saline were used as the control (black curve). *P < 0.005 when compared to saline control.

In addition, we have also evaluated toxicity of the developed nanoparticles on the specific organs by measuring serum biomarkers that are commonly used in preclinical and clinical studies as well as in routine clinical care [56]. To evaluate the activatable SiNc-PNP for its effect on renal, heart, and liver toxicity, we measured concentrations of surrogate markers in blood for kidney function (blood urea nitrogen (BUN) and creatinine); heart function (creatine kinase (CK)); and liver function (alanine transaminase (ALT) and alkaline phosphatase (ALP)). The measured values in non-treated mice (control) and mice injected with the SiNc-NP were similar, suggesting that our nanoplatform is safe (Figures 9B and C).

Phototoxicity of a patient's skin under sunlight is a clinically significant side effect of phototherapy [57]. To test if SiNc-NP is photosafe, nude mice were injected simultaneously i.v. and subcutaneously (sub-Q) with SiNc-NP and exposed to simulated sunlight for 2 h daily for 7 days (10,000 lux). No changes in behavior, weight loss, skin damage (such as redness, burns, etc.) were observed, indicating that SiNc-loaded NPs are photosafe and do not cause phototoxicity or photosensitivity under simulated sunlight (Figures 9D and E). In addition, we evaluated genotoxicity of the developed nanoplatform. Figure 9F exhibits the representative microscopic images of stained cells treated with media (negative control), MMS (positive control), and SiNc-PNPs. Most cell nuclei had the clear and smooth edge in the negative control group treated with media only, whereas noticeable numbers of small buds/fragments appeared on/near cell nuclei, representing micronuclei, in the positive group treated with MMS. These images also showed that most cell nuclei remained intact when treated with SiNc NPs. A quantitative analysis was then performed to evaluate the genotoxicity by counting the number of micronuclei per 1000 cells. Compared to the negative control, SiNc-loaded NPs did not induce more formation of micronuclei, suggesting no genotoxicity observed at the tested NP concentration.

Conclusions

We have successfully developed a single agent-based theranostic nanoplatform that primarily activates its NIR fluorescence at the tumor site, but not in systemic circulation or healthy organs. Initially, the hydrophobic core of the nanoparticle is densely packed with SiNc molecules causing a self-quenching effect and the turning off of NIR fluorescence of SiNc. After accumulation at the tumor site and internalization into cancer cells, the theranostic nanoparticles start dissociating in the intracellular environment, and thus cause destruction of the tight dye packing inside PNP, thereby activating the NIR fluorescence inside the tumor. Based on our results, we assumed that the acidic environment of cancer tumors and the interior of the endosome/lysosome can partially contribute to the activation of SiNc-PNP

fluorescence by disrupting the integrity of self-assembled PEG-PCL nanoparticles, thereby inducing SiNc release from the hydrophobic core. Furthermore, the detected low internalization efficiency of SiNc-PNP into the non-malignant cells explains their ability to generate none or minimal fluorescence signal in healthy organs. The developed nanoparticles were successfully delivered to, accumulated at, and even penetrated into the core of tumors in animal models. Subsequently, these activatable SiNc-encapsulated polymeric nanoparticles turned on their NIR fluorescence at the tumor site, offering high cancer-to-tissue contrast imaging. The tumor targeting and imaging capability of activatable SiNc-PNP was validated in two different murine xenograft models including an intraperitoneal metastasis-mimicking model. Remarkably, the feasibility of activatable SiNc-PNP in the application of real-time intraoperative image-guided surgery was demonstrated using Fluobeam® 800, an FDA-approved intraoperative NIR imaging system, during which sensitive fluorescence detection of cancer tumors was observed for tumor resection. In addition, this nanoplatform features intrinsic advantages for implementation as a personalized nanomedicine. First of all, the switching profile broadens the imaging and treatment window,

making it flexible for personalization. Secondly, the SiNc-mediated combinatorial phototherapy process can be tailored via photo irradiation dosage. Overall, the revealed properties of the activatable SiNc-PNP make it highly promising for further application in clinical image-guided surgery and combined phototherapy, facilitating a potential translation to clinical studies.

Abbreviations

NIR: near infrared; SiNc: silicon naphthalol-cyanine; PNP: polymeric nanoparticles; PEG-PCL: (poly (ethylene glycol)-*b*-poly(ε-caprolactone); ICG: indocyanine green; FDA: Food & Drug Administration; THF: tetrahydrofuran; DLS: dynamic light scattering; cryoTEM: cryogenic transmission electron microscopy; FITC: fluorescein isothiocyanate; IACUC: the Institutional Animal Care and Use Committee; DMSO: dimethyl sulfoxide; ROI: regions of interest; T/N: tumor-to-normal tissue ratio; F.I.: fluorescence intensity; SDS: sodium dodecyl sulfate; ROS: reactive oxygen species; MMS: methyl methanesulfonate; BUN: blood urea nitrogen; CK: creatine kinase; ALT: alanine transaminase; ALP: alkaline phosphatase.
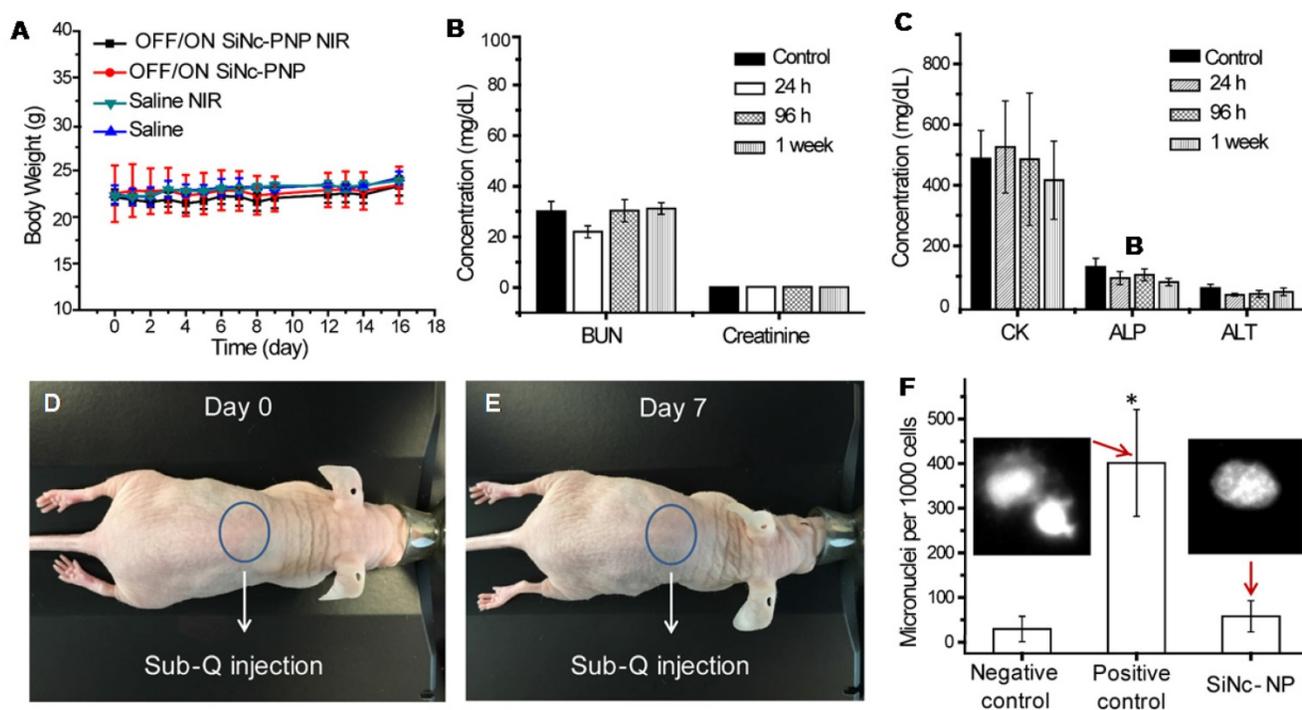

Figure 9. (A) Changes in body weights of treated mice compared to control groups. **(B)** and **(C)** The blood levels of BUN and creatinine, illustrating kidney function; CK, illustrating cardiac function; and ALT and ALP, illustrating liver function, in control mice and mice injected i.v. with the activatable (OFF/ON) SiNc-PNP, assessed after 24 h, 96 h and 1 week. **(D, E)** Images of nude mice, illustrating the lack of phototoxicity (skin damage). **(F)** An *in vitro* micronucleus assay (formation of micronuclei) was used to determine the genotoxicity of the activatable SiNc-PNP. CHO-K1 cells were treated with the activatable SiNc-PNP (90 µg/mL) for the experiment group, fresh media for negative control, or methyl methanesulfonate (MMS, 50 µg/mL) for a positive control. Inset: fluorescence images of CHO-K1 cells nuclei treated for 24 h with MMS (left) and activatable SiNc-PNP (right). *P < 0.05 when compared with positive control (media).

Acknowledgements

Supplementary Material

Real-time videos of activatable SiNc-PNP mediated image-guided surgery; characterization methods; *in vivo* images; experimental toxicity methods, etc. Supplementary information and Figure S1.
http://www.thno.org/v08p0767s1.pdf
Video S1. http://www.thno.org/v08p0767s2.avi
Video S2. http://www.thno.org/v08p0767s3.avi

Competing Interests

The authors have declared that no competing interest exists.

References

1. Frangioni JV. New technologies for human cancer imaging. J Clin Oncol. 2008; 26: 4012-21.
2. Berg WA, Gutierrez L, NessAiver MS, Carter WB, Bhargavan M, Lewis RS, et al. Diagnostic accuracy of mammography, clinical examination, US, and MR imaging in preoperative assessment of breast cancer. Radiology. 2004; 233: 830-49.
3. Kiesslich R, Burg J, Vieth M, Gnaendiger J, Enders M, Delaney P, et al. Confocal laser endoscopy for diagnosing intraepithelial neoplasias and colorectal cancer in vivo. Gastroenterology. 2004; 127: 706-13.
4. Lardinois D, Weder W, Hany TF, Kamel EM, Korom S, Seifert B, et al. Staging of non-small-cell lung cancer with integrated positron-emission tomography and computed tomography. N Engl J Med. 2003; 348: 2500-7.
5. Bartholf DeWitt S, Eward WC, Eward CA, Lazarides AL, Whitley MJ, Ferrer JM, et al. A novel imaging system distinguishes neoplastic from normal tissue during resection of soft tissue sarcomas and mast cell tumors in dogs. Vet Surg. 2016; 45: 715-22.
6. Nguyen QT, Tsien RY. Fluorescence-guided surgery with live molecular navigation-a new cutting edge. Nat Rev Cancer. 2013; 13: 653-62.
7. Belghiti J, Panis Y, Farges O, Benhamou JP, Fekete F. Intrahepatic recurrence after resection of hepatocellular carcinoma complicating cirrhosis. Ann Surg. 1991; 214: 114-7.
8. Quigley MR. Early postoperative magnetic resonance imaging after resection of malignant glioma: objective evaluation of residual tumor and influence on regrowth and prognosis. Neurosurgery. 1994; 34: 1105.
9. Vahrmeijer AL, Hutteman M, van der Vorst JR, van de Velde CJ, Frangioni JV. Image-guided cancer surgery using near-infrared fluorescence. Nat Rev Clin Oncol. 2013; 10: 507-18.
10. Chi C, Du Y, Ye J, Kou D, Qiu J, Wang J, et al. Intraoperative imaging-guided cancer surgery: from current fluorescence molecular imaging methods to future multi-modality imaging technology. Theranostics. 2014; 4: 1072-84.
11. van Dam GM, Themelis G, Crane LM, Harlaar NJ, Pleijhuis RG, Kelder W, et al. Intraoperative tumor-specific fluorescence imaging in ovarian cancer by folate receptor-alpha targeting: first in-human results. Nat Med. 2011; 17: 1315-9.
12. Lee BT, Hutteman M, Gioux S, Stockdale A, Lin SJ, Ngo LH, et al. The FLARE intraoperative near-infrared fluorescence imaging system: a first-in-human clinical trial in perforator flap breast reconstruction. Plast Reconstr Surg. 2010; 126: 1472-81.
13. Sugie T, Sawada T, Tagaya N, Kinoshita T, Yamagami K, Suwa H, et al. Comparison of the indocyanine green fluorescence and blue dye methods in detection of sentinel lymph nodes in early-stage breast cancer. Ann Surg Oncol. 2013; 20: 2213-8.
14. Troyan SL, Kianzad V, Gibbs-Strauss SL, Gioux S, Matsui A, Oketokoun R, et al. The FLARE intraoperative near-infrared fluorescence imaging system: a first-in-human clinical trial in breast cancer sentinel lymph node mapping. Ann Surg Oncol. 2009; 16: 2943-52.
15. Crane LM, Themelis G, Pleijhuis RG, Harlaar NJ, Sarantopoulos A, Arts HJ, et al. Intraoperative multispectral fluorescence imaging for the detection of the sentinel lymph node in cervical cancer: a novel concept. Mol Imaging Biol. 2011; 13: 1043-9.
16. van der Vorst JR, Hutteman M, Gaarenstroom KN, Peters AA, Mieog JS, Schaafsma BE, et al. Optimization of near-infrared fluorescent sentinel lymph node mapping in cervical cancer patients. Int J Gynecol Cancer. 2011; 21: 1472-8.
17. van der Vorst JR, Schaafsma BE, Hutteman M, Verbeek FP, Liefers GJ, Hartgrink HH, et al. Near-infrared fluorescence-guided resection of colorectal liver metastases. Cancer. 2013; 119: 3411-8.
18. Fujiwara M, Mizukami T, Suzuki A, Fukamizu H. Sentinel lymph node detection in skin cancer patients using real-time fluorescence navigation with indocyanine green: preliminary experience. J Plast Reconstr Aesthet Surg. 2009; 62: e373-8.
19. Crane LM, Themelis G, Arts HJ, Buddingh KT, Brouwers AH, Ntziachristos V, et al. Intraoperative near-infrared fluorescence imaging for sentinel lymph node detection in vulvar cancer: first clinical results. Gynecol Oncol. 2011; 120: 291-5.
20. Hutteman M, van der Vorst JR, Gaarenstroom KN, Peters AA, Mieog JS, Schaafsma BE, et al. Optimization of near-infrared fluorescent sentinel lymph node mapping for vulvar cancer. Am J Obstet Gynecol. 2012; 206: 89 e1-5.
21. Li Y, Lin TY, Luo Y, Liu Q, Xiao W, Guo W, et al. A smart and versatile theranostic nanomedicine platform based on nanoporphyrin. Nat Commun. 2014; 5: 4712.
22. Frangioni JV. In vivo near-infrared fluorescence imaging. Curr Opin Chem Biol. 2003; 7: 626-34.
23. Weissleder R. A clearer vision for in vivo imaging. Nat Biotechnol. 2001; 19: 316-7.
24. Matsui A, Tanaka E, Choi HS, Winer JH, Kianzad V, Gioux S, et al. Real-time intra-operative near-infrared fluorescence identification of the extrahepatic bile ducts using clinically available contrast agents. Surgery. 2010; 148: 87-95.
25. Schaafsma BE, Mieog JS, Hutteman M, van der Vorst JR, Kuppen PJ, Lowik CW, et al. The clinical use of indocyanine green as a near-infrared fluorescent contrast agent for image-guided oncologic surgery. J Surg Oncol. 2011; 104: 323-32.
26. Ishizawa T, Fukushima N, Shibahara J, Masuda K, Tamura S, Aoki T, et al. Real-time identification of liver cancers by using indocyanine green fluorescent imaging. Cancer. 2009; 115: 2491-504.
27. Urano Y, Asanuma D, Hama Y, Koyama Y, Barrett T, Kamiya M, et al. Selective molecular imaging of viable cancer cells with pH-activatable fluorescence probes. Nat Med. 2009; 15: 104-9.
28. Shimizu S, Kamiike W, Hatanaka N, Yoshida Y, Tagawa K, Miyata M, et al. New method for measuring ICG Rmax with a clearance meter. World J Surg. 1995; 19: 113-8.
29. Haughland RP. Handbook of fluorescent probes and research chemicals. Eugene, OR, USA: Molecular Probes Inc. 2002.
30. Duong T, Li X, Yang B, Schumann C, Albarqi HA, Taratula O, et al. Phototheranostic nanoplatform based on a single cyanine dye for image-guided combinatorial phototherapy. Nanomedicine. 2016; 13: 955-63.
31. Maeda H, Nakamura H, Fang J. The EPR effect for macromolecular drug delivery to solid tumors: Improvement of tumor uptake, lowering of systemic toxicity, and distinct tumor imaging in vivo. Adv Drug Deliv Rev. 2013; 65: 71-9.
32. Lee S, Cha EJ, Park K, Lee SY, Hong JK, Sun IC, et al. A near-infrared-fluorescence-quenched gold-nanoparticle imaging probe for in vivo drug screening and protease activity determination. Angew Chem Int Ed Engl. 2008; 47: 2804-7.
33. Liu L, Ma G, Zhang C, Wang H, Sun H, Wang C, et al. An activatable theranostic nanomedicine platform based on self-quenchable indocyanine green-encapsulated polymeric micelles. J Biomed Nanotechnol. 2016; 12: 1223-33.
34. Wang Y, Zhou K, Huang G, Hensley C, Huang X, Ma X, et al. A nanoparticle-based strategy for the imaging of a broad range of tumours by nonlinear amplification of microenvironment signals. Nat Mater. 2014; 13: 204-12.
35. Taratula O, Doddapaneni BS, Schumann C, Li X, Bracha S, Milovancev M, et al. Naphthalocyanine-based biodegradable polymeric nanoparticles for image-guided combinatorial phototherapy. Chem of Mater. 2015; 27: 6155-65.
36. Keereweer S, Van Driel PB, Snoeks TJ, Kerrebijn JD, Baatenburg de Jong RJ, Vahrmeijer AL, et al. Optical image-guided cancer surgery: challenges and limitations. Clin Cancer Res. 2013; 19: 3745-54.
37. Marsden HR, Gabrielli L, Kros A. Rapid preparation of polymersomes by a water addition/solvent evaporation method. Polym Chem. 2010; 1: 1512-8.
38. Schumann C, Chan S, Khalimonchuk O, Khal S, Moskal V, Shah V, et al. Mechanistic nanotherapeutic approach based on siRNA-mediated DJ-1 protein suppression for platinum-resistant ovarian cancer. Mol Pharm. 2016; 13: 2070-83.

39. Taratula O, Schumann C, Duong T, Taylor KL, Taratula O. Dendrimer-encapsulated naphthalocyanine as a single agent-based theranostic nanoplatform for near-infrared fluorescence imaging and combinatorial anticancer phototherapy. Nanoscale. 2015; 7: 3888-902.

40. Katayose M, Tai S, Kamijima K, Hagiwara H, Hayashi N. Novel silicon naphthalocyanines - synthesis and molecular arrangement in thin-films. J Chem Soc-Perkin Trans 2. 1992: 403-9.

41. Petrasek Z, Phillips D. A time-resolved study of concentration quenching of disulfonated aluminium phthalocyanine fluorescence. Photochem Photobiol Sci. 2003; 2: 236-44.

42. Lee SJ, Koo H, Lee DE, Min S, Lee S, Chen X, et al. Tumor-homing photosensitizer-conjugated glycol chitosan nanoparticles for synchronous photodynamic imaging and therapy based on cellular on/off system. Biomaterials. 2011; 32: 4021-9.

43. Chen H, Kim S, Li L, Wang S, Park K, Cheng JX. Release of hydrophobic molecules from polymer micelles into cell membranes revealed by Forster resonance energy transfer imaging. Proc Natl Acad Sci USA. 2008; 105: 6596-601.

44. Cuong NV, Jiang JL, Li YL, Chen JR, Jwo SC, Hsieh MF. Doxorubicin-Loaded PEG-PCL-PEG Micelle Using Xenograft Model of Nude Mice: Effect of multiple administration of micelle on the suppression of human breast cancer. Cancers (Basel). 2010; 3: 61-78.

45. Sorkin A, Von Zastrow M. Signal transduction and endocytosis: close encounters of many kinds. Nat Rev Mol Cell Biol. 2002; 3: 600-14.

46. Gatenby RA, Gillies RJ. A microenvironmental model of carcinogenesis. Nat Rev Cancer. 2008; 8: 56-61.

47. Mauro N, campora S, Adamo G, Scialabba C, Ghersi G, Giammona G. Polyaminoacid–doxorubicin prodrug micelles as highly selective therapeutics for targeted cancer therapy. RSC Adv. 2016; 6: 77256-66.

48. Han Y, Li S, Cao X, Yuan L, Wang Y, Yin Y, et al. Different inhibitory effect and mechanism of hydroxyapatite nanoparticles on normal cells and cancer cells in vitro and in vivo. Sci Rep. 2014; 4: 7134.

49. Commisso C, Davidson SM, Soydaner-Azeloglu RG, Parker SJ, Kamphorst JJ, Hackett S, et al. Macropinocytosis of protein is an amino acid supply route in Ras-transformed cells. Nature. 2013; 497: 633-7.

50. Mosesson Y, Mills GB, Yarden Y. Derailed endocytosis: an emerging feature of cancer. Nat Rev Cancer. 2008; 8: 835-50.

51. Mellman I, Yarden Y. Endocytosis and cancer. Cold Spring Harb Perspect Biol. 2013; 5: a016949.

52. Sahay G, Kim JO, Kabanov AV, Bronich TK. The exploitation of differential endocytic pathways in normal and tumor cells in the selective targeting of nanoparticulate chemotherapeutic agents. Biomaterials. 2010; 31: 923-33.

53. Jiang ZP, Zhu ZS, Liu CJ, Hu Y, Wu W, Jiang XQ. Non-enzymatic and enzymatic degradation of poly(ethylene glycol)-b-poly-(epsilon-caprolactone) diblock copolymer micelles in aqueous solution. Polymer 2008; 49: 5513-9.

54. Shi B, Fang C, You MX, Zhang Y, Fu SK, Pei YY. Stealth MePEG-PCL micelles: effects of polymer composition on micelle physicochemical characteristics, in vitro drug release, in vivo pharmacokinetics in rats and biodistribution in S-180 tumor bearing mice. Colloid Polym Sci 2005; 282: 954-67.

55. Zhang J, Chen X, Shi G, Xie X, Liu H, Zhang X, et al. Establishment of a new representative model of human ovarian cancer in mice. J Ovarian Res. 2013; 6: 9.

56. Campion S, Aubrecht J, Boekelheide K, Brewster DW, Vaidya VS, Anderson L, et al. The current status of biomarkers for predicting toxicity. Expert Opin Drug Metab Toxicol. 2013; 9: 1391-408.

57. Steinbauer J, Schreml S, Karrer S, Ackermann G, Babilas P, Landthaler M, et al. Phototoxic reactions in healthy volunteers following photodynamic therapy with methylaminolevulinate cream or with cream containing 5-aminolevulinic acid: a phase II, randomized study. Photodermatol Photoimmunol Photomed. 2009; 25: 270-5.